A study on biorelevant calciprotein particles: Effect of stabilizing agents on the formation and crystallization mechanisms

A study on biorelevant calciprotein particles: effect of stabilizing agents on the formation and crystallization mechanisms

Rita Gelli, Valentina Pucci, Francesca Ridi*, Piero Baglioni

Department of Chemistry "Ugo Schiff" and CSGI, University of Florence,
via della Lastruccia 3, 50019 Sesto Fiorentino, Florence, Italy

Corresponding author
Francesca Ridi
E-mail: francesca.ridi@unifi.it Tel: +39 055 4573015
Address: Department of Chemistry "Ugo Schiff" and CSGI, University of Florence, via della Lastruccia 3, Sesto Fiorentino, 50019 Florence, Italy.

Abstract

Hypothesis: Calciprotein particles (CPPs) are endogenous nanoparticles consisting of hybrid mineral-organic colloidal complexes made of calcium phosphates and Fetuin-A (Fet-A), a protein that in physiological conditions binds to amorphous calcium phosphate forming primary CPP (CPP1). CPP1 can crystallize resulting in hydroxyapatite-based secondary CPP (CPP2) that can eventually precipitate leading to vascular calcifications. The treatment of patients with molecules and ions that delay the amorphous-to-crystalline transition has shown promising results from a clinical perspective, but the study of their mechanism of action has not been thoroughly examined so far.

Experiments: This work describes the formation and crystallization mechanism of synthetic analogs of endogenous CPPs. The effect of different concentrations of Fet-A and of stabilizing agents (Mg^{2+}, citrate and pyrophosphate) on the features and stability of CPPs was addressed by combining different characterization

Abbreviations: HA: Hydroxyapatite; Fet-A: Fetuin-A; CPPs: Calciprotein Particles; CPMs: Calciprotein Monomers; CPP1: Primary Calciptorein particles; CPP2: Secondary Calciprotein Particles; VC: Vascular Calcifications; TRIS: Tris(hydroxymethyl)aminomethane; DLS: Dynamic Light Scattering; D_h: Hydrodynamic Diameter; PDI: Polydispersity Index; SD: Standard Deviation; FT-IR: Fourier Transform Infrared Spectroscopy; XRD: X-Ray Diffraction; FWHM: Full Width at Half Maximum; FE-SEM: Field Emission-Scanning Electron Microscopy; EDX: Energy Dispersive X-Rays spectroscopy.

techniques such as turbidimetry, dynamic light scattering, infrared spectroscopy, and scanning electron microscopy.

Findings: The results show that the stabilizing agents display different action mechanisms and are effective to a different extent in preventing the formation of CPPs or delaying their crystallization. Such findings could be of interest to develop effective therapies for vascular calcifications and to deepen the understanding of amorphous calcium phosphate stabilization and its interaction with proteins.

Graphical abstract

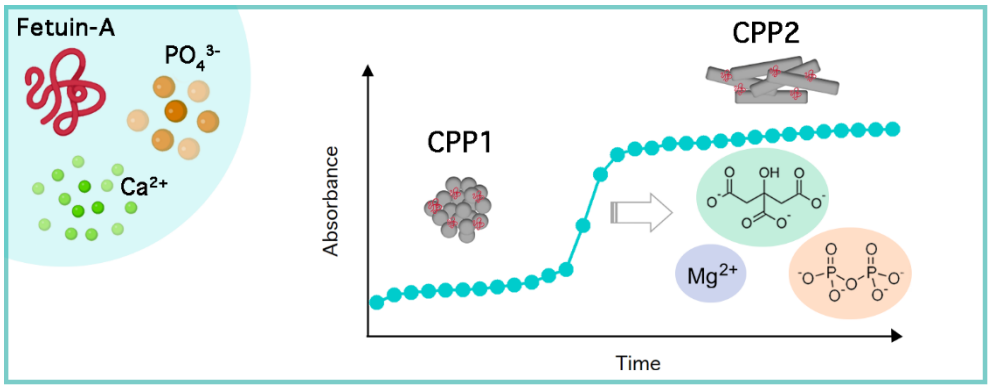

Keywords

Calciprotein particles; Fetuin-A; Nanoparticles; Proteins; Calcium phosphates; Magnesium; Citrate; Pyrophosphate; Stability; Crystallization.

1 Introduction

The formation of calcium phosphates in our body is a fascinating and complex phenomenon that requires the coordination of multiple mechanisms to achieve mineralization in specific locations, such as bones and teeth [1]. Ectopic calcifications, *i.e.* inappropriate biomineralization in soft tissues [2], can occur in various conditions, such as aging, cancer, diabetes, atherosclerosis and chronic kidney diseases [3].

Despite the concentration of calcium and phosphate ions in serum is in the supersaturated regime for the formation of hydroxyapatite (HA), in physiological conditions the precipitation of this mineral in blood does not take place due to the presence of inhibitors of either crystal nucleation or growth [4]. Among such molecules and macromolecules, Fetuin-A (Fet-A) is a liver-derived glycoprotein that is the main responsible

for the prevention of serum calcification. Also known as α_2-Heremans Schmid glycoprotein [1], Fet-A circulates in blood at about 0.8 mg/mL (~15 μM), which is about 1/40 than physiological albumin levels [5]. Albumin is the most abundant serum protein, and it is also involved in the inhibition of calcification, since it interacts with Ca^{2+} ions with its acidic amino acid residues lowering Ca^{2+} effective concentration [1]. The mechanism of action of Fet-A is different and more effective, as it binds to nascent clusters formed by calcium and phosphate ions via its negatively charged β-sheet within the amino-terminal cystatin-like D1 domain, acting as a barrier that prevents their aggregation and growth [1]. The colloidal hybrid mineral-organic complexes made of calcium phosphates and Fet-A are called calciprotein particles (CPPs) and have been characterized at different stages, *i.e.* CPP1 and CPP2. The initial interaction of Fet-A with Ca^{2+} and phosphate ions leads to calciprotein monomers (CPMs) that aggregate forming primary calciprotein particles (CPP1) [6]. CPP1 are small colloidal nanoparticles made of amorphous calcium phosphate with a diameter below 100 nm [7]. In physiological conditions, such small nanoparticles are considered harmless and can be easily cleared from the circulation [8]; nevertheless, in case of disturbed mineral homeostasis or impeded clearance (typical in patients suffering from chronic kidney diseases [6]), they undergo structural rearrangement into larger secondary calciprotein particles (CPP2) which consist of needle-like crystals of HA [9] that can precipitate and initiate pathological situations. CPP2 can be internalized by vascular cells, thus leading to proinflammatory effects and calcification of vascular smooth muscle cells [10]. Moreover, CPP2 are also connected to atherosclerosis and vascular calcifications (VC), which are depositions of calcium phosphate crystals in the arterial walls or aortic valves [11] that might eventually result in cardiovascular diseases, the major cause for death worldwide [12,13].

The understanding of CPPs' formation mechanism and crystallization pathway as well as their physiological and pathological role is key to develop specific therapeutic strategies. So far, CPPs have been reported in the serum of patients' [14–16] or from their precipitation by supersaturated solutions of calcium and phosphate salts [5,17]. The latter approach allows the *in vitro* study of the formation and crystallization processes, and the evaluation of how different factors, such as Fet-A concentration [17,18], affect the endogenous-like pathway.

It is though that CPPs' amorphous-to-crystalline transition needs further investigation and that future clinical trials should be addressed to the study of crystallization inhibitors of CPP2 [8]. The latter aspect is particularly

relevant, as factors reducing calcification propensity are of interest in the context of clinical management of VC [19]. Such factors, together with temperature, pH, concentration of Fet-A, albumin, Ca^{2+} and phosphate ions [6,19,20], also include ions and molecules that might slow down the CPP1 to CPP2 transition [12]. Several studies have shown that the oral supplementation [21–25] or inclusion in dialysate media [26,27] of magnesium are effective in reducing calcification serum propensity, suggesting that magnesium supplementation might be a promising treatment option for VC. Few studies have addressed the mechanism underneath this clinical observation, particularly important is the study of Pasch *et al.* [20] and the recent works of ter Braake *et al.* [19,28]. Besides magnesium, citrate has proven effective to reduce the risk of VC in clinical applications [24,29–31], but no studies analyzed the mechanism of action towards CPP-like systems besides calcification propensity tests. The effect of citrate is of interest as this ion is also involved in bone remodeling, where it is thought to act as apatite stabilizer [4]. Another ion involved in bone remodeling is pyrophosphate, which is an endogenous mineralization inhibitor that participates to the control of ectopic calcifications [32]: studies show that the defective synthesis of pyrophosphate promotes the surge of VC [33] while its supplementation might have beneficial effects in inhibiting VC [21,34]. Interestingly, all the ions which have shown a clinical effectiveness are also involved in the *in vitro* stabilization of amorphous calcium phosphate [35–40] and are therefore expected to affect the CPP1 to CPP2 transition. Nevertheless, the precise pathway of action of these ions has not be explored from a physico-chemical approach, as most studies only rely on the assessment of their effect on the serum calcification propensity (*i.e.* T_{50} test, a nephelometric assay that measures CPP formation by supersaturating patients' serum with calcium and phosphate [20]).

The aim of this work is the study of the formation and crystallization mechanisms of synthetic analogs of endogenous CPP from a physico-chemical perspective, focusing on the effect of Fet-A concentration and of the presence of different calcification inhibitors, namely Mg^{2+}, citrate and pyrophosphate. Synthetic analogs of endogenous CPPs were obtained *in vitro* and the crystallization (or *ripening*) mechanism was studied *in situ* by combining turbidimetry with dynamic light scattering. To highlight the possible different mechanisms of action of the stabilizing agents with respect to CPP formation or stability, particles were collected at selected time intervals and analyzed in terms of crystallinity, morphology, elemental composition, and at different Fet-A concentrations as well as in the presence of different amounts of Mg^{2+}, citrate and pyrophosphate.

2 Materials and methods

2.1 Materials

NaCl (purity > 99.5 %), $CaCl_2$ (purity > 93.0 %), $Na_2HPO_4 \cdot 12H_2O$ (purity > 99.0 %), $MgCl_2 \cdot 6H_2O$ (purity > 99.0 %), $Na_4P_2O_7 \cdot 10H_2O$ (purity > 99.0 %), $Na_3C_6H_5O_7 \cdot 2H_2O$ (purity > 99.0 %) and Fetuin from fetal bovine serum (M_w 48,400 g/mol) were purchased from Sigma Aldrich. Tris(hydroxymethyl)aminomethane (TRIS, purity > 99.7 %) was obtained from Fluka while HCl 37 % from Carlo Erba Reagents. Milli-Q water (resistivity 18.2 MΩ·cm) was used throughout all the experiments.

2.2 Preparation of CPPs at different Fet-A concentrations

CPPs were prepared following a protocol reported in the literature [5], schematized in Figure S1. TRIS (0.303 g) was dissolved in 50 mL of water to obtain a 50 mM solution. The pH (pH meter 7+ with DHS electrode, XS instruments) was lowered from the initial value of about 10 to 7.40 by dropwise addition of HCl 1 M. $CaCl_2$ (0.022 g) and NaCl (0.164 g) were dissolved in 10 mL of the TRIS 50 mM solution, yielding to $[Ca^{2+}]$ = 20 mM and $[Na^+]$ = 280 mM (solution A). 0.043 g of $Na_2HPO_4 \cdot 12H_2O$ were dissolved in 10 mL of the 50 mM TRIS solution, resulting in a concentration of phosphate 12 mM (solution B). Fet-A was dissolved in solution B to obtain a 30 µM solution (14.5 mg in 10 mL), which was properly diluted with B to obtain [Fet-A] = 10 and 20 µM. CPPs were obtained upon mixing at 37 °C equal volumes of solution A and solution B at different [Fet-A]. The concentrations in the final volume were therefore $CaCl_2$ 10 mM, NaCl 140 mM, Na_2HPO_4 6 mM and Fet-A 0 µM (sample F0), 5 µM (sample F5), 10 µM (sample F10) and 15 µM (sample F15). For the characterization of dried powders, aliquots (5 mL) were centrifuged (Neya 16R, REMI, A6-50 rotor) at 8000 rpm for 5 min, then washed with 5 mL of water and centrifuged again in the same conditions. The precipitate was frozen in liquid nitrogen and lyophilized for 24 h (VirTis benchtop freeze-dryer).

2.3 Preparation of CPPs at different Mg^{2+} concentrations

The preparation of CPPs was conducted in the presence of different concentrations of Mg^{2+} (0, 1, 5 and 10 mM) at 0 and 5 µM of Fet-A. Briefly, 4.07 mg, 20.35 mg and 40.7 mg of $MgCl_2 \cdot 6H_2O$ were each dissolved in 10 mL of solution A (see section 2.2), in order to obtain solutions at $[Mg^{2+}]$ = 2 mM, 10 mM and 20 mM, respectively. 9.68 mg of Fet-A were dissolved in 20 mL of solution B (see section 2.2) obtaining a 10 µM solution. CPPs were obtained by mixing at 37 °C 5 mL of solution A (at the four different Mg^{2+} concentrations) with either 5 mL of solution B or 5 mL of solution B including Fet-A. Eight samples were therefore obtained

by combining the four different Mg^{2+} concentrations (0, 1, 5 and 10 mM) with [Fet-A] = 0 and 5 µM. Sample's nomenclature is reported in Table 1, where X=M. Aliquots were collected as described in section 2.2.

Table 1. Composition of samples investigated in this work.

Sample	[Fet-A] (µM)*	[X-Additive]† (mM)*
F0	0	0
F5	5	0
F10	10	0
F15	15	0
F0_X0	0	0
F0_X1	0	1
F0_X5	0	5
F0_X10	0	10
F5_X0	5	0
F5_X1	5	1
F5_X5	5	5
F5_X10	5	10

* The concentrations refer to the final volume in solution

†[X-Additive] = M: magnesium, C: citrate, P: pyrophosphate

2.4 Preparation of CPPs at different citrate concentrations

The synthesis of CPPs was performed in the presence of four different concentrations of trisodium citrate (0, 1, 5 and 10 mM) without or with 5 µM Fet-A. 20 mL of solution A were prepared as described in section 2.2. In parallel, 50 mL of solution B (see section 2.2) were prepared, and 9.68 mg of Fet-A were dissolved in 20 mL of it, obtaining a 10 µM solution. $Na_3C_6H_5O_7 \cdot 2H_2O$ (2.94 mg, 14.7 mg and 29.4 mg) were dissolved in 5 mL of either solution B or solution B including Fet-A, in order to obtain 2 mM, 10 mM and 20 mM citrate solutions, with and without Fet-A. 5 mL of solution A were mixed at 37 °C with 5 mL of solutions B at different citrate concentrations to obtain CPPs. Eight samples were therefore prepared by combining the four different

citrate concentrations (0, 1, 5 and 10 mM) with [Fet-A] = 0 and 5 μM. Sample's nomenclature is reported in Table 1, where X=C. Aliquots were collected as described in section 2.2.

2.5 Preparation of CPPs at different pyrophosphate concentrations

CPPs in the presence of pyrophosphate were obtained following the same procedure described for citrate in section 2.4, the only difference being the amount of $Na_4P_2O_7 \cdot 10H_2O$: 4.46 mg, 22.3 mg and 44.6 mg in 5 mL of solution B or solution B with Fet-A. Sample's nomenclature is reported in Table 1, where X=P.

2.6 Characterization techniques

2.6.1 Turbidimetry

The ripening process of CPPs was monitored by means of turbidimetry, using a Cary 3500 spectrophotometer (Agilent). Immediately after mixing, the dispersions were transferred in plastic cuvettes and placed in the spectrophotometer. Samples were analyzed at 37 °C for 16 h by recording the absorbance at 400 nm every 2 min [5]. An integration time of 0.020 s and a bandwidth of 1 nm were used to collect the absorbance data. 50 mM solution of TRIS was used as reference.

2.6.2 Dynamic Light Scattering (DLS)

DLS measurements were performed at 37 °C with a Particle Size Analyzer 90 Plus (Brookhaven Instruments). Immediately after mixing, the dispersions were placed in a cuvette and the autocorrelation functions were acquired by averaging 10 runs of 10 s each. Each sample was monitored every 15 min for 3 h. Samples in the presence of Mg^{2+} were monitored up to 1 week. The autocorrelation functions were fitted with the cumulant method [41], and the hydrodynamic diameters (D_h) and polydispersity indexes (PDI) were obtained as averages of 10 runs. PDI, according to the instrument manual, is defined as:

$$PDI = \left(\frac{half\ width}{mean}\right)^2 \qquad \text{Equation 1}$$

The standard deviation (SD) was calculated according to the relationship:

$$half\ width = 2 \cdot SD\sqrt{2ln2} \approx 2.35 \cdot SD \qquad \text{Equation 2}$$

2.6.3 Fourier Transform-Infrared Spectroscopy (FT-IR)

FT-IR spectra were collected with a Bio-Rad FTS-40 spectrophotometer. The freeze-dried samples were analyzed in KBr pellets, which were prepared with (1.00 ± 0.05) mg of sample and (100 ± 1) mg of KBr

(Sigma-Aldrich, FT-IR grade). Each spectrum was acquired in the range 4000-400 cm^{-1}, with resolution 2 cm^{-1}, 64 scans and with scan delay 600 s. A KBr pellet was subtracted to each spectrum as a blank.

2.6.4 X-Ray Diffraction (XRD)

XRD patterns were collected with a D8 Advance with DAVINCI design (Bruker), using as X-rays source the Cu Kα radiation (wavelength λ=1.54 Å), at 40 kV and 40 mA. The diffractograms were acquired using a 2θ range of 5°-60°, a step size of 0.03°, and a time/step of 0.3 s. Freeze-dried samples were grinded using mortar and pestle and flattened onto a Si zero-background sample holder.

Scherrer equation (Equation 3) was used to calculate the crystalline domain size (D, nm):

$$D = \frac{\kappa\lambda}{\beta\cos(\theta)} \qquad \text{Equation 3}$$

where κ is the Scherrer constant, typically considered 0.9, λ is the X-Ray wavelength (nm), β is the FWHM (Full Width at Half Maximum) in radians and θ is the diffraction angle in radians [42]. The FWHM were obtained from the Multi-Peak Fitting routine of the software IgorPro. The peak at 26° was considered for the analysis.

2.6.5 Field Emission-Scanning Electron Microscopy (FE-SEM) coupled with Energy Dispersive X-Rays spectroscopy (EDX)

FE-SEM micrographs were collected using a Zeiss ΣIGMA FE-SEM (Carl Zeiss Microscopy GmbH). The freeze-dried samples were placed on aluminum stubs using conductive tape. The use of a Field Emission source with a low accelerating voltage (2 kV), a reduced sample-detector distance (~2 mm) and the In-Lens detector allowed for the imaging of non-metallized samples. The size distributions were calculated measuring the diameter of 250 particles *per* sample, using the software ImageJ. EDX was carried out using X-act Silicon Drift Detector (Oxford Instruments, England). To collect EDX spectra, the accelerating voltage was 10 kV, while the working distance was ~8 mm. Elemental atomic % ratios are expressed as average ± standard deviation of 3 different sites on each sample.

3 Results

3.1 Effect of Fet-A concentration

The effect of different concentrations of Fet-A in the CPP synthetic medium was initially evaluated. This aspect is particularly important as Fet-A levels in blood were shown to be fundamental for the inhibition of ectopic mineralization, as mice deficient in this protein suffer from soft tissue calcifications [21,43,44]. Useful insights about the effect of the protein were obtained by observing the turbidity and the stability of the suspensions at (37 ± 1) °C (Figure 1A), correlating them with turbidimetric curves (Figure 1B). Turbidimetry is a useful technique to monitor the size evolution and the stability of particles in suspension, as the amount of scattered light is related to the size of the objects in the dispersion. When the solution containing calcium ions is mixed with the one containing phosphates (see section 2.2), in the absence of Fet-A a very turbid suspension is immediately obtained, and the precipitation of the inorganic phase begins within few minutes. This is evident by looking at the sample on the left in Figure 1A, and its corresponding turbidimetric curve (green one in Figure 1B), which shows an initial abrupt increase followed by a rapid decrease in absorbance, reaching zero after about 1 h. When Fet-A is present in the synthetic medium, a marked stabilizing action is observed. The turbidimetric curves of Fet-A containing samples show a sigmoidal shape, with an initial stage where the absorbance gradually rises, followed by a steep increase that leads to a plateau region. The onset time of this transition (see Figure 1C) is 24 min, 34 min and 54 min for samples F5, F10 and F15, respectively. These values show a linear relationship with the concentration of Fet-A (see Figure 1D). The turbidimetric curve of sample F5 (red in Figure 1A) also displays an abrupt decrease in absorbance (after about 3 h) which indicates the precipitation of the dispersion. On the other hand, in samples F10 and F15 the absorbance remains constant for the whole duration of the experiment (16 h, see the complete curves in Figure S2). Moreover, the absorbance in the plateau region is higher for sample F15 (0.8) than F10 (0.6), which might suggest the presence of larger objects in suspension in the former sample. Nevertheless, as the turbidity of a suspension is a function of both the number of particles and their size distribution [45], it is also possible that the higher amount of protein in F15 stabilizes a higher amount of particles in such sample.

The results from turbidimetric analysis are confirmed by the macroscopic appearance of the samples in Figure 1A, showing that samples F10 and F15 are stable up to 46 h. For sample F10, the precipitation process begins after 56 h of incubation, whereas for F15 a precipitate is observed after 70 h. Heiss *et al.* reports that with Fet-A above 7 µM, CPP2 dispersions are stable for more than 2 days while with 5 µM the sedimentation begins after about 2 h [5]. We found that the sedimentation for sample F5 starts before 2 h, likely due to the different

temperature at which the experiments were carried out (37 °C to better mimic physiological environment). We also monitored the sedimentation process for longer time, finding that 15 µM of Fet-A make the CPP2 suspension stable for more than 56 h.

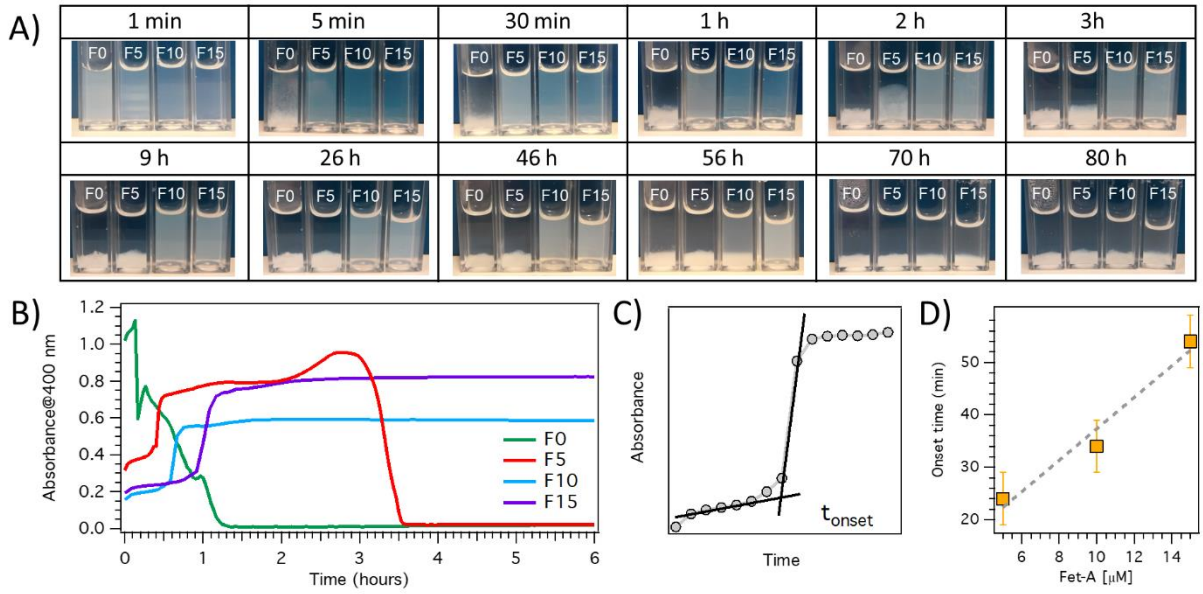

Figure 1. A) Photos of the dispersions incubated at 37 °C (time indicates the time elapsed from the beginning of mixing). B) Turbidimetric curves of the samples up to 6 h (the trend up to 16 h is reported in Figure S2). C) Example of calculation of the onset time of the transition (t_{onset}). D) Plot of the onset time vs Fet-A concentration in the dispersion. The error bars are ± 5 min and indicate the variation of the onset time obtained in three replicated experiments for sample F5.

In order to study the size of the particles formed in solution at the various stages of the process, the samples were analyzed in situ by means of DLS, collecting the autocorrelation functions after 5 min from the mixing and every 15 min, for 3 h. Even after 5 min, sample F0 is not stable and cannot be analyzed by means of DLS. On the contrary, the autocorrelation functions for samples containing Fet-A after 5 min from the mixing (see a representative example in Figure 2A) can be fitted using cumulant analysis, showing particles with hydrodynamic diameters (D_h) of (136 ± 20) nm, (115 ± 12) nm and (122 ± 17) nm for F5, F10 and F15, respectively (see also Table 2, SD calculated from PDI). The evolution of D_h in time is reported in Figure 2B. In sample F5 the size of the particles abruptly increases after about 30 min while for both F10 and F15 D_h gradually increases after about 60 min, reaching about 200 nm. These results well agree with the onset times observed by turbidimetry. The values of D_h obtained for F10 and F15 are very similar (e.g., after 3 h D_h= (206

± 36) nm for F10 and (195 ± 28) nm for F15), suggesting that the absorbance observed in turbidimetry curves (see Figure 1B), which is higher for F15 than F10, might be connected to a greater particles' number rather than to larger particles' size.

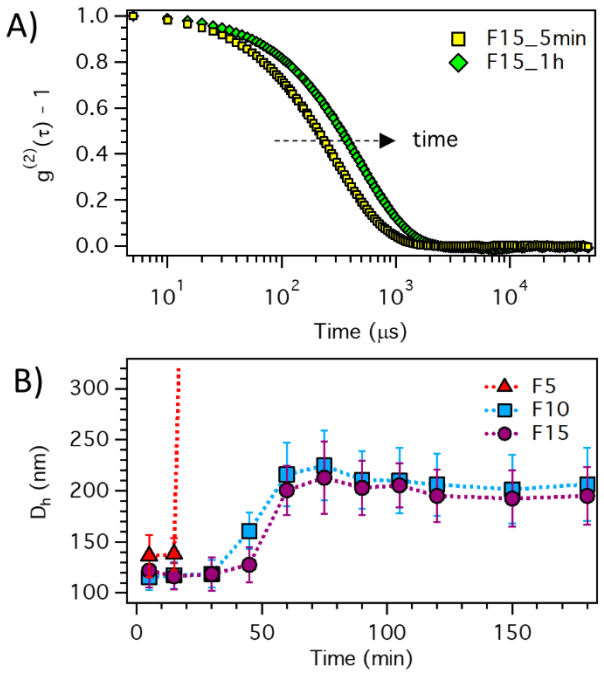

Figure 2. A) Representative normalized autocorrelation functions (sample F15 after 5 min and 1 h). B) Plot of the hydrodynamic diameter as a function of reaction time (F5: triangles; F10: squares; F15: circles). The error bars are the standard deviations calculated according to the polydispersity (see Equation 1 and 2).

The chemical nature and the morphology of the particles formed in solution was examined by collecting aliquots by means of centrifugation and freeze-drying. FT-IR results from samples after 5 min and 16 h reaction are reported in Figure 3. The spectrum of samples prepared with Fet-A and collected after 5 min (see Figure 3A) is in agreement with amorphous calcium phosphate [46]. On the contrary, sample F0 presents a splitting of the 580 cm^{-1} peak suggesting the presence of poorly crystalline HA [47]. All samples collected after 16 h are compatible with poorly crystalline HA (see Figure 3B). Interestingly, samples with and without protein differ as an additional peak at about 1540 cm^{-1} is present only for samples prepared with Fet-A (see the panel in Figure 3). The intensity of the peak at about 1650 cm^{-1}, due to water bending in calcium phosphates, is also stronger in samples with protein. These signals are compatible with Fet-A main peaks (see Figure S3) and

indicate the presence of the protein on both amorphous and crystalline particles. The protein is likely strongly bound to the surface of the nanoparticles as it is detected even if the particles were washed before the freeze-drying procedure.

The crystallinity of the samples was further analyzed by means of XRD. The diffractograms of the 5 min samples in Figure 3C and of the 16 h samples in Figure 3D confirm FT-IR results, showing a pattern compatible with poorly crystalline HA for F0_5min, F0_16h, F5_16h, F10_16h and F15_16h, while a profile typical of amorphous calcium phosphate for F5_5min, F10_5min and F15_5min is observed [47]. The crystallinity degree was assessed using the Scherrer equation (see section 2.6.4) on the (0 0 2) peak of the pattern (2θ=26°) [48] and the crystallite sizes are reported in Table S1: sample F0 increases its crystallinity in time (crystallite size 21 nm at 5 min vs 35 nm at 16 h), while all samples at 16 h show a similar degree of crystallinity (34 ± 1 nm), compatible with values reported in the literature for bone HA [49].

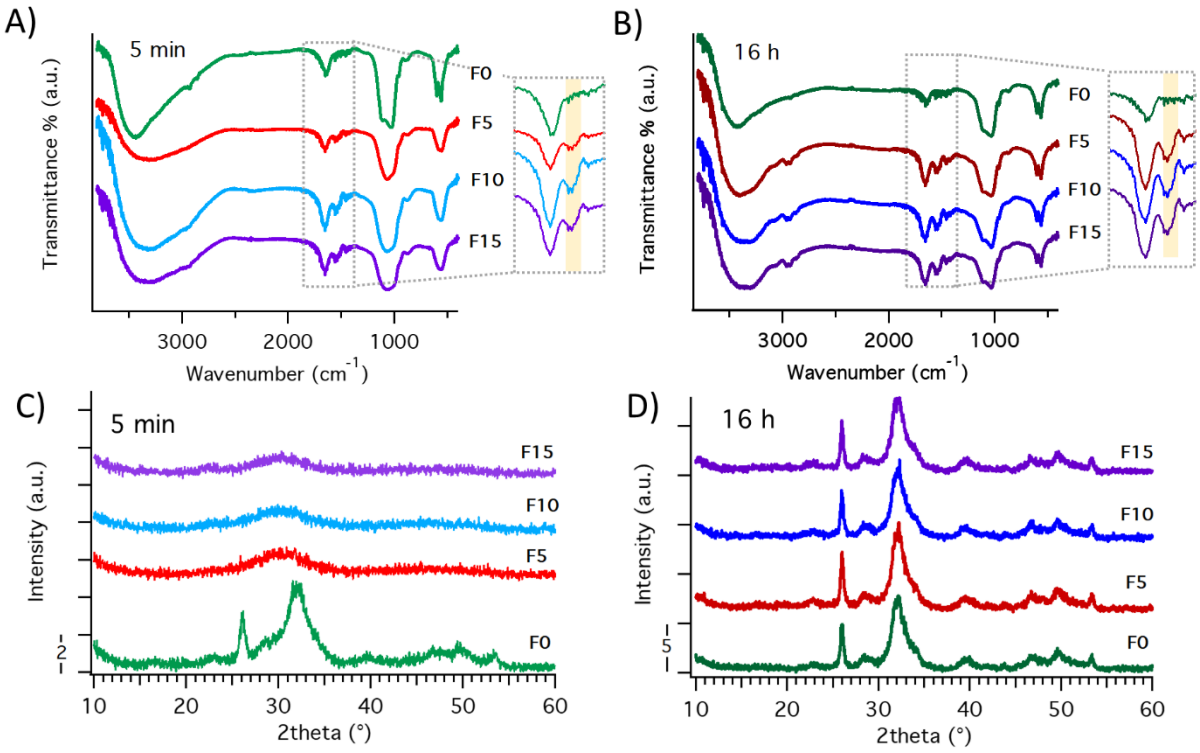

Figure 3. FT-IR spectra of particles collected after 5 min (A) and 16 h (B). XRD patterns of particles collected after 5 min (C) and 16 h (D). All curves are offset for display purposes.

Figure 4 reports the FE-SEM morphology of the particles after 5 min and 16 h. Samples at 5 min reaction time show spherical morphology; however, significant differences are observed when Fet-A is present in the

reaction medium. F0 presents polydisperse objects whose single units (about 82 nm in diameter, see Figure S4 and Table 2) are clustered, explaining the observed immediate precipitation in the reaction medium (see Figure 1A). On the other hand, samples F5, F10 and F15 consist of more spherical nanoparticles which have size similar to F0 (see Table 2) but are aggregated to a much lesser extent and have a more regular shape. Ca/P ratios as obtained by means of EDX spectroscopy show in all cases values around 1.2, compatible with amorphous calcium phosphate (see Table S2) [50].

After 16 h, F0 displays a flake-like morphology, typical of poorly crystalline HA [51], while samples F5, F10 and F15 show needle-like nanoparticles. The length of such needles is in the 100-200 nm range, while typical widths are few tens of nm, consistently with the D_h values after ripening previously discussed.

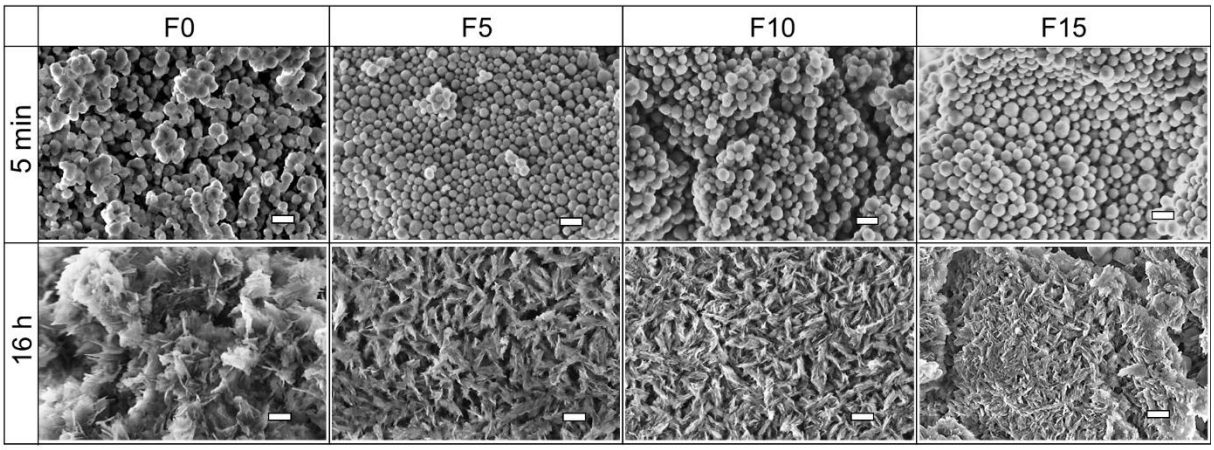

Figure 4. FE-SEM micrographs of samples collected after 5 min (top row) and 16 h (bottom row). Each column corresponds to sample F0, F5, F10 and F15. The scale bar is 200 nm for all images.

Table 2. Comparison of the features of the particles collected after 5 min. Diameter and SD are obtained as average value and standard deviation from FE-SEM size distribution curves, reported in the Supplementary Material (average of 250 particles *per* sample). D_h and PDI refer to DLS measurements (average out of 10 runs for each sample), and the SD was calculated from PDI according to Equation 1 and 2. For the ripening time, data were obtained by turbidimetry except for F5_M5 and F5_M10, where the increase in diameter observed by DLS was considered.

	FE-SEM	DLS	Turbidimetry/DLS

Sample	Diameter ± SD (nm)	Morphology	D_h ± SD (nm)	PDI	Ripening time
F0_5min	82 ± 25*	Spherical, aggregated	-	-	-
F5_5min	72 ± 20	Spherical	136 ± 20	0.12 ± 0.03	24 min
F10_5min	65 ± 16	Spherical	115 ± 12	0.06 ± 0.01	34 min
F15_5min	85 ± 25	Spherical	122 ± 17	0.10 ± 0.02	54 min
F5_M1_5min	91 ± 21	Spherical	141 ± 20	0.11 ± 0.03	119 min
F5_M5_5min	78 ± 18	Spherical	158 ± 21	0.10 ± 0.02	~21 h
F5_M10_5min	80 ± 18	Spherical	158 ± 21	0.10 ± 0.02	~ 103 h
F5_C1_5min	80 ± 26	Spherical	193 ± 30	0.11 ± 0.01	72 min
F5_C5_5min	55 ± 12	Spherical	204 ± 28	0.11 ± 0.02	~3 h

* Size of the single units present in the micrographs, not the aggregates size.

These results show that the endogenous pathway of CPPs was successfully reproduced: the initial amorphous spherical nanoparticles of diameter below 100 nm (*i.e.*, CPP1) ripen, increase their size and crystallize, forming needle-shaped HA nanocrystals (*i.e.,* CPP2) that eventually precipitate. The role of Fet-A in this scenario was outlined, showing that the protein delays the onset time of the ripening process in a concentration-dependent fashion. Moreover, when the concentration is equal to 10 and 15 μM, Fet-A can efficiently stabilize the colloidal suspensions of CPP2, which precipitate after 56 h and 70 h, respectively. These two distinct aspects are connected but should be discussed separately, as we speculate that the inhibitory role of Fet-A towards ectopic mineralization can take place with two mechanisms: *i)* extended stability of CPP1, which are less pathogenic than CPP2 [6], or *ii)* colloidal stability of CPP2 that prevents precipitation and therefore the formation of vascular calcifications. Comparing these two effects it appears that high concentrations of Fet-A mostly affect the *ii)* process, as increasing the concentration from Fet-A 5 μM to 15 μM the onset time increases from 24 min to 54 min, while the beginning of the sedimentation process increases from 2 h to 70 h.

3.2 Effect of stabilizing agents

3.2.1 Mg^{2+}

The preparation of CPPs was conducted by varying the amount of magnesium in the reacting medium, keeping constant the concentration of Fet-A at 5 µM. Such protein concentration was chosen to mimic a potential pathological situation where Fet-A might be lacking, so to analyze if the inclusion of stabilizing agents could restore the role of the "missing" Fet-A or even be more effective (we recall that physiological levels of Fet-A are about 15 µM [5]). All experiments were carried out with Mg^{2+}concentration of 0, 1, 5 and 10 mM without and with 5 µM of Fet-A.

The turbidimetry curves are shown in Figure 5A. In the absence of Fet-A, the absorbance immediately drops as all samples quickly precipitate, irrespectively of Mg^{2+} concentration. When 5 µM of protein is present in the medium, the effect of Mg^{2+} is evident: for 1 mM Mg^{2+}, the onset time of the ripening process is delayed of almost 5 times with respect to the sample without Mg^{2+} (119 min for F5_M1 vs 24 min for F5_M0). At higher Mg^{2+} concentrations, the absorbance is constant throughout the experiment, suggesting that no ripening phenomena occur over 16 h (the complete set of data is reported in Figure S5A). This is consistent with the samples' appearance at the end of the experiment reported in Figure S5B that shows turbid suspensions for F5_M5 and F5_M10, whereas the other samples are precipitated.

The evolution of the systems was also studied by means of DLS, and the plot of the hydrodynamic diameter in time is given in Figure 5B. In this case, samples were monitored up to 10 days, to get a complete overview of the ripening process. Samples without Fet-A could not be analyzed by means of DLS due to the quick precipitation. For 5 µM Fet-A, a different behavior according to the concentration of Mg^{2+} is observed: D_h of sample F5_M1 abruptly increases after 120 min of incubation, in agreement with turbidimetry results. As expected, F5_M5 and F5_M10 are constant in size for more than 16 h, which is the timeframe examined by means of turbidimetry: D_h increases after 32 h for the sample F5_M5, and precipitates after 45 h, whereas for the sample F5_M10, D_h significantly rises only after 189 h and precipitates after 237 h.

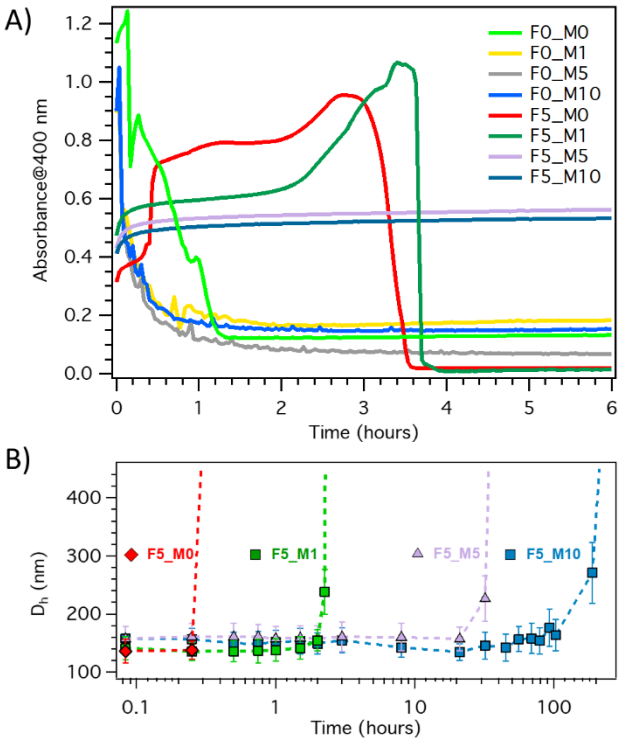

Figure 5. A) Turbidimetry curves of samples for 0 µM Fet-A and 5 µM and 0, 1, 5 and 10 mM Mg^{2+}. B) Plot of the hydrodynamic diameter vs incubation time. The error bars are the standard deviations calculated according to the polydispersity (see Equation 1 and 2).

Samples collected after 5 min and 16 h were also analyzed by means of FT-IR (Figure S6). All 5 min samples except for F0_M0 show an infrared spectrum compatible with amorphous calcium phosphate, as expected. After 16 h, samples at low Mg^{2+} concentration (*i.e.*, 0 and 1 mM) consist of poorly crystalline HA, both with and without Fet-A. When 5 mM of Mg^{2+} is present, the system is crystalline without the protein but amorphous when 5 µM of Fet-A is in the reaction medium. Finally, 10 mM Mg^{2+} results in amorphous samples both with and without Fet-A. The crystallinity of the 16 h samples was confirmed by means of XRD (see Figure S7): the pattern of F5_M0_16h and F5_M1_16h is compatible with poorly crystalline hydroxyapatite with a similar crystallinity degree (see Table S1), whereas F5_M5_16h and F5_M10_16h display a profile typical of amorphous calcium phosphate. These observations are in agreement with FE-SEM analysis reported in Figure S8 (5 min samples), and S9 (16 h samples). F5 samples prepared in the presence of Mg^{2+} and collected after 5 min show the typical morphology of CPP1 with an average size slightly larger than F5_M0 (see Table 2 and the size distribution curves in Figure S10). In contrast, analogous samples prepared without Fet-A display the

typical morphology of amorphous nanoparticles but are aggregated to a much larger extent (Figure S8, top row). Ca/P ratios are again compatible with amorphous calcium phosphate while Ca/Mg ratios suggest that a small amount of Mg is included in the nanoparticles, its amount increasing with the concentration in the reaction medium (see Table S3).

Samples collected after 16 h show the typical morphology of poorly crystalline HA, except for F0_M10, F5_M5 and F5_M10 which, in agreement with FT-IR analysis, are still amorphous. The crystallization of such samples likely occurs at later times. DLS analysis revealed that the ripening process occurs after about 2 days for sample F5_M5 and 8 days for F5_M10. FT-IR showed that the crystallization process eventually occurs in samples incubated for 10 days (see Figure S11).

In summary, data show that rather than affecting the initial formation of amorphous CPP1, Mg^{2+} delays the ripening process to CPP2 in a concentration-dependent fashion. Mg^{2+} influence on the stabilization of amorphous calcium phosphates is well known [35,51,52], and is likely the responsible for the observed effects. It is important to point out that a synergic effect between Mg^{2+} and Fet-A likely occurs, as samples F0_M5 and F5_M5 incubated for 16 h are crystalline and amorphous, respectively (see Figure S6 and S9).

As pointed out, Fet-A is more effective in preventing crystalline CPP2 precipitation rather than delaying the transition from CPP1 to CPP2: the action of Mg^{2+} is somehow the opposite, since its effect is focused on the inhibition of the crystallization process. If we recall that normal physiological Mg^{2+} concentrations in blood is 0.7–1.1 mM [19], we can speculate that supplementations might be effective in extending CPP1 lifetime and, reasonably, in preventing the surge of VC.

3.2.2 Citrate

The role of citrate in CPPs formation and ripening was examined by conducting experiments with 0, 1, 5 and 10 mM of tri-sodium citrate, without and with 5 µM of Fet-A. Turbidimetry curves in Figure S12 show that samples without Fet-A quickly precipitate (F0_C0, F0_C1 and F0_C5). Interestingly, the absorbance of samples with 10 mM of citrate (both with and without protein) is 0 throughout the whole experiment and no calcium phosphate forms in such a media. F5_C1 shows a steep increase in absorbance that occurs at longer time with respect to F5_C0 (72 min vs 24 min), suggesting a mild action of citrate in delaying the ripening process. The precipitation of the system is also observed, as absorbance rapidly goes to zero after about 3.5 h.

In contrast to the other samples, F5_C5 does not display a marked increase in absorbance but rather a slow and constant rise until 3 hours. After this lag time, the precipitation process begins.

DLS measurements were performed in order to further analyze the ripening process (see Figure 6). Again, samples without Fet-A could not be analyzed due to immediate precipitation upon mixing of the precursor's solutions. Both F5_C1 and F5_C5 show an initial D_h of about 200 nm, larger than that of samples prepared without additives and with Mg^{2+} (see Table 2): this effect might be due to citrate adsorption on the surface of CPP that increase the hydration shell. The D_h of citrate-CPPs is constant up to about 90 min (see Figure 6A and 6B). We recall that sample F5 without any additive begins to increase its size after about 30 min (see Figure 2), confirming the effect of citrate in stabilizing CPP1. Sample F5_C1 shows an abrupt increase in size and reaches a D_h above 1.5 µm at 2 h. Interestingly, when 5 mM of citrate is present (*i.e.*, sample F5_C5), the ripening mechanism is different, as the size of the nanoparticles gradually increases (see Figure 6C). These results are in very good agreement with turbidimetry as F5_C1 shows an abrupt increase in absorbance while F5_C5 displays a slow and gradual increase in the absorbance value (see Figure S12).

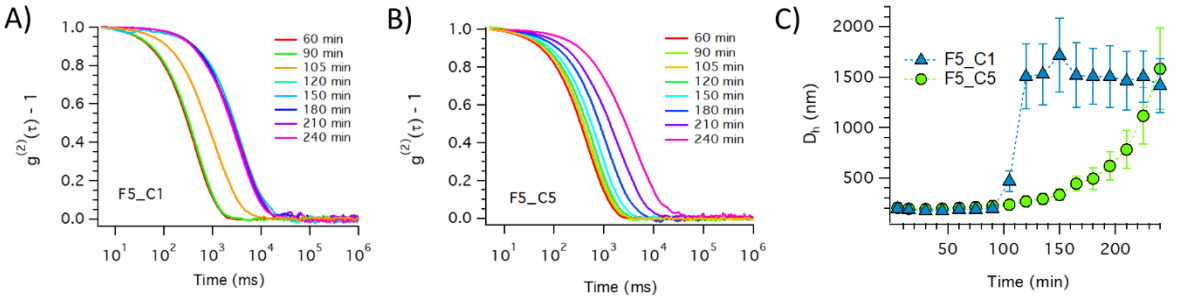

Figure 6. DLS results for CPPs prepared in the presence of citrate. A) Normalized autocorrelation functions of sample F5_C1 in time; B) Normalized autocorrelation functions of sample F5_C5 as a function of time; C) Plot of the hydrodynamic diameter vs time of samples F5_C1 (blue triangles) and F5_C5 (green circles). The error bars are the standard deviations calculated according to the polydispersity (see Equation 1 and 2).

Particles at 5 min and 16 h were collected and analyzed by means of FE-SEM and FT-IR. FE-SEM results of particles collected after 5 min reported in Figure S13 show that the presence of 5 mM of citrate leads to the formation of slightly smaller particles than with 1 mM, both with and without protein (see Figure S14 and Table 2). This evidence supports the hypothesis that the higher D_h observed for this sample with DLS might be due to an increase of the hydration shell rather than to a larger size of the inorganic core. The Ca/P ratio of

all the 5 min samples is consistent with amorphous calcium phosphate, as reported in Table S4. The morphology of samples collected after 16 h is compatible with poorly crystalline HA, as shown in Figure S15. FT-IR spectra are in agreement with SEM observations, being compatible with either amorphous calcium phosphate or HA (see Figure S16). The crystallinity degree of samples collected after 16 h was assessed using Scherrer method (Equation 3) analyzing the XRD diffractograms reported in Figure S17. Interestingly, the crystallite size decreases as citrate amount in the reacting solution increases (35 nm for F5_C0_16h, 31 nm for F5_C1_16h and 28 nm for F5_C5_16h, see Table S1), confirming once again the effect of this ion in delaying the amorphous-to-crystalline transition in calcium phosphates.

All data taken together suggest that citrate displays a mild stabilizing effect towards CPP1: when present at 1 mM and 5 mM, it delays the conversion process from CPP1 to CPP2, even though different mechanisms are in play, as suggested by DLS analysis. A high concentration of citrate (*i.e.* 10 mM) completely prevents the precipitation of any type of calcium phosphate, likely due to the chelating effect of citrate on Ca^{2+}. Citrate is in fact administrated to patients suffering from calcium-based kidney stones due to its action in inhibiting calcium phosphate stone formation through multiple mechanisms, including the formation of soluble citrate–calcium complexes, and the inhibition of CaP nucleation, crystal growth and crystal aggregation [53].

3.2.3 Pyrophosphate

Experiments analogous to those conducted for Mg^{2+} and citrate were also carried out for pyrophosphate. Turbidimetry results are shown in Figure 7A: interestingly, when pyrophosphate is present in the CPP synthetic solution, the absorbance is nearly constant during the 16 h experiment, differently from the typical behavior observed for the CPP1 to CPP2 transition (*i.e.*, the green curve in Figure 7A). The only exception is sample F0_P1, that quickly precipitates. Samples observation at the end of the experiment (Figure S18) shows that most samples consist of a turbid dispersion that entraps air bubbles, which is likely responsible for the behavior observed in turbidimetric curves. DLS measurements conducted on samples after 5 min from the mixing show that in all systems the size of the objects present in solution is above the range accessible by the instrument (data not shown). This occurred both in the presence and in the absence of the protein. These results suggest that when pyrophosphate is present in the reaction medium the formation of the CPP is prevented, and a different type of inorganic solid precipitates. To assess this, samples collected after 5 min and 16 h were

analyzed through FE-SEM and FT-IR. SEM micrographs show that the morphology of 5 min samples (Figure S19) is analogous to that of 16 h samples (Figure S20), in agreement with turbidimetry results. All samples, irrespectively of pyrophosphate concentration and of the presence of protein, consist of very small objects that form an aggregated mesh-like structure, markedly different from that of CPP1 or CPP2 (see a representative micrograph in Figure 7B). The Ca/P ratio measured by EDX of both 5 min and 16 h samples reported in Table S5 is close to 1, in agreement with the stoichiometry of calcium pyrophosphates ($Ca_2P_2O_7$). FT-IR results reported in Figure S21 confirmed that in such a system the formation of CPP1 and CPP2 does not occur, as the spectra of all samples are consistent with amorphous calcium pyrophosphate [54]. To further confirm this hypothesis, selected samples were analyzed by means of XRD, and the results are given in Figure 7C. In fact, while the pattern of sample F5_P0_16h is compatible with that of poorly-crystalline HA [47], both samples F5_P1 and F5_P10 showed the diffractogram typical of amorphous structures that is again in agreement with the formation of amorphous calcium pyrophosphate [54].

In summary, the presence of pyrophosphate in CPP synthetic medium completely prevents the formation of CPP1, as amorphous calcium pyrophosphate forms in all analyzed systems, both with and without protein and at all the investigated pyrophosphate concentrations.

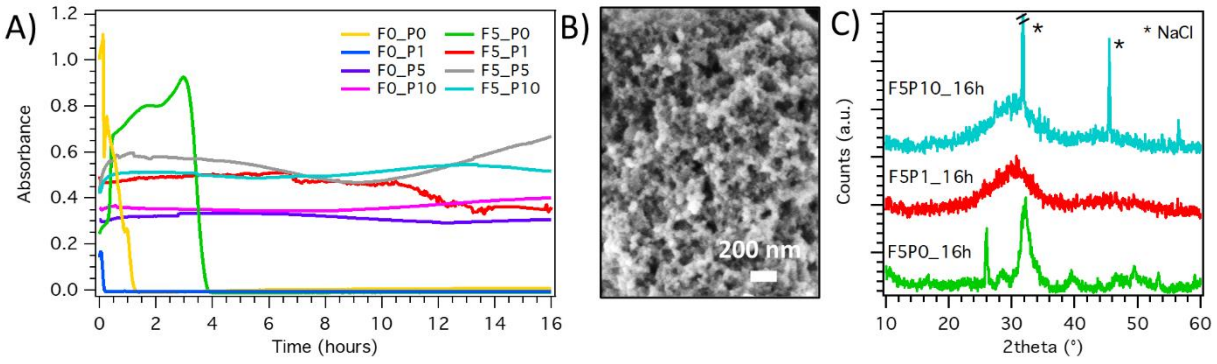

Figure 7. A) Turbidimetry curves of samples in the presence of different concentrations of pyrophosphate; B) FE-SEM micrograph of sample F5_P10_16h; C) XRD patterns of samples (from bottom to top) F5_P0_16h, F5_P1_16h, F5_P10_16h. The diffractograms are offset for display purposes. The sharp peaks present in F5_P10_16h are due to residual NaCl from synthetic medium [55].

5 Conclusions

This work addresses the effect of different Fet-A concentrations and stabilizing agents (Mg^{2+}, citrate and pyrophosphate) on the formation and crystallization mechanism of calciprotein particles made of calcium phosphates stabilized by Fet-A. The effect of different protein concentrations was studied by combining turbidimetry and DLS, that allowed monitoring the in situ evolution of the system, together with the analysis of the morphology and crystallinity of the nanoparticles using SEM and FT-IR. Results show the initial formation of CPP1, amorphous calcium phosphate spherical nanoparticles below 100 nm, that abruptly increase their size resulting in CPP2, needle-like HA, that eventually precipitate, replicating the endogenous pathway. The concentration of Fet-A affects both the onset time of the transition from CPP1 to CPP2 and the colloidal stability of CPP2. Analogous experiments were carried out in the presence of 1, 5 and 10 mM of stabilizing agent, at constant amount of Fet-A. Results show that rather than affecting the initial formation of amorphous CPP1, Mg^{2+} delays the ripening process to CPP2 in a concentration-dependent fashion, leading to a remarkable preservation of the amorphous phase up to 8 days. The effect of citrate is milder, while pyrophosphate completely prevents CPP formation because of the preferential precipitation of amorphous calcium pyrophosphate.

The results presented in this work improve the knowledge of the inhibition mechanisms of the investigated additives in terms of effect towards CPP formation or CPP1 to CPP2 transition, corroborating the clinical findings outlined in the Introduction section. The most effective additive in preventing CPP1 to CPP2 transition is Mg^{2+}, probably due to its efficiency in stabilizing amorphous calcium phosphates [35,51,56]. These findings could be significant not only to develop effective therapies to treat vascular calcifications but could also be of interest for researchers working on the stabilization of amorphous phosphates and on the formation of organic-inorganic hybrid structures. Future studies could take into account the investigation of the Fet-A-nanoparticle interface and the design of clinical studies to compare the effectiveness of the three stabilizers and corroborate these findings.

Acknowledgements

CSGI consortium, MUR PRIN - 2017249YEF and MIUR-Italy ("Progetto Dipartimenti di Eccellenza 2018-2022" allocated to Department of Chemistry "Ugo Schiff") are acknowledged for financial support.

References

[1] M.M.X. Cai, E.R. Smith, S.G. Holt, The role of fetuin-A in mineral trafficking and deposition, BoneKEy Rep. 4 (2015) 672. https://doi.org/10.1038/bonekey.2015.39.

[2] C.M. Giachelli, Ectopic Calcification, Am. J. Pathol. 154 (1999) 671–675. https://doi.org/10.1016/S0002-9440(10)65313-8.

[3] T.-Y. Wong, H.-H. Peng, C.-Y. Wu, J. Martel, D.M. Ojcius, F.-Y. Hsu, J.D. Young, Nanoparticle conversion to biofilms: in vitro demonstration using serum-derived mineralo-organic nanoparticles, Nanomed. 10 (2015) 3519–3535. https://doi.org/10.2217/nnm.15.171.

[4] N. Vidavsky, J.A.M.R. Kunitake, L.A. Estroff, Multiple Pathways for Pathological Calcification in the Human Body, Adv. Healthc. Mater. (2020) 2001271. https://doi.org/10.1002/adhm.202001271.

[5] A. Heiss, T. Eckert, A. Aretz, W. Richtering, W. van Dorp, C. Schäfer, W. Jahnen-Dechent, Hierarchical Role of Fetuin-A and Acidic Serum Proteins in the Formation and Stabilization of Calcium Phosphate Particles, J. Biol. Chem. 283 (2008) 14815–14825. https://doi.org/10.1074/jbc.M709938200.

[6] C.N. Silaghi, T. Ilyés, A.J. Van Ballegooijen, A.M. Crăciun, Calciprotein Particles and Serum Calcification Propensity: Hallmarks of Vascular Calcifications in Patients with Chronic Kidney Disease, J. Clin. Med. 9 (2020) 1287. https://doi.org/10.3390/jcm9051287.

[7] W. Jahnen-Dechent, A. Büscher, S. Köppert, A. Heiss, M. Kuro-o, E.R. Smith, Mud in the blood: the role of protein-mineral complexes and extracellular vesicles in biomineralisation and calcification, J. Struct. Biol. 212 (2020) 107577. https://doi.org/10.1016/j.jsb.2020.107577.

[8] Kutikhin Anton G., Feenstra Lian, Kostyunin Alexander E., Yuzhalin Arseniy E., Hillebrands Jan-Luuk, Krenning Guido, Calciprotein Particles, Arterioscler. Thromb. Vasc. Biol. 41 (2021) 1607–1624. https://doi.org/10.1161/ATVBAHA.120.315697.

[9] E.R. Smith, T.D. Hewitson, W. Jahnen-Dechent, Calciprotein particles: mineral behaving badly?, Curr. Opin. Nephrol. Hypertens. 29 (2020) 378–386. https://doi.org/10.1097/MNH.0000000000000609.

[10] P. Aghagolzadeh, M. Bachtler, R. Bijarnia, C. Jackson, E.R. Smith, A. Odermatt, R. Radpour, A. Pasch, Calcification of vascular smooth muscle cells is induced by secondary calciprotein particles and enhanced by tumor necrosis factor-α, Atherosclerosis. 251 (2016) 404–414. https://doi.org/10.1016/j.atherosclerosis.2016.05.044.

[11] Y. Tintut, H.M. Honda, L.L. Demer, Biomolecules Orchestrating Cardiovascular Calcification, Biomolecules. 11 (2021) 1482. https://doi.org/10.3390/biom11101482.

[12] A.E. Schantl, M.E. Ivarsson, J.-C. Leroux, Investigational Pharmacological Treatments for Vascular Calcification, Adv. Ther. 2 (2019) 1800094. https://doi.org/10.1002/adtp.201800094.

[13] A.E. Schantl, A. Verhulst, E. Neven, G.J. Behets, P.C. D'Haese, M. Maillard, D. Mordasini, O. Phan, M. Burnier, D. Spaggiari, L.A. Decosterd, M.G. MacAskill, C.J. Alcaide-Corral, A.A.S. Tavares, D.E. Newby, V.C. Beindl, R. Maj, A. Labarre, C. Hegde, B. Castagner, M.E. Ivarsson, J.-C. Leroux, Inhibition of vascular calcification by inositol phosphates derivatized with ethylene glycol oligomers, Nat. Commun. 11 (2020) 721. https://doi.org/10.1038/s41467-019-14091-4.

[14] P.A. Price, T.M.T. Nguyen, M.K. Williamson, Biochemical Characterization of the Serum Fetuin-Mineral Complex, J. Biol. Chem. 278 (2003) 22153–22160. https://doi.org/10.1074/jbc.M300739200.

[15] J. Martel, D. Young, A. Young, C.-Y. Wu, C.-D. Chen, J.-S. Yu, J.D. Young, Comprehensive proteomic analysis of mineral nanoparticles derived from human body fluids and analyzed by liquid chromatography–tandem mass spectrometry, Anal. Biochem. 418 (2011) 111–125. https://doi.org/10.1016/j.ab.2011.06.018.

[16] M.M. Cai, B. Wigg, E.R. Smith, T.D. Hewitson, L.P. McMahon, S.G. Holt, Relative abundance of fetuin-A in peritoneal dialysis effluent and its association with in situ formation of calciprotein particles: An observational pilot study, Nephrology. 20 (2015) 6–10. https://doi.org/10.1111/nep.12350.

[17] C.N. Rochette, S. Rosenfeldt, A. Heiss, T. Narayanan, M. Ballauff, W. Jahnen-Dechent, A Shielding Topology Stabilizes the Early Stage Protein–Mineral Complexes of Fetuin-A and Calcium Phosphate: A Time-Resolved Small-Angle X-ray Study, ChemBioChem. 10 (2009) 735–740. https://doi.org/10.1002/cbic.200800719.

[18] J. Wald, S. Wiese, T. Eckert, W. Jahnen-Dechent, W. Richtering, A. Heiss, Formation and stability kinetics of calcium phosphate–fetuin-A colloidal particles probed by time-resolved dynamic light scattering, Soft Matter. 7 (2011) 2869–2874. https://doi.org/10.1039/C0SM01191F.

[19] A.D. ter Braake, M.G. Vervloet, J.H.F. de Baaij, J.G.J. Hoenderop, Magnesium to prevent kidney disease–associated vascular calcification: crystal clear?, Nephrol. Dial. Transplant. (2020) gfaa222. https://doi.org/10.1093/ndt/gfaa222.

[20] A. Pasch, S. Farese, S. Gräber, J. Wald, W. Richtering, J. Floege, W. Jahnen-Dechent, Nanoparticle-Based Test Measures Overall Propensity for Calcification in Serum, J. Am. Soc. Nephrol. 23 (2012) 1744–1752. https://doi.org/10.1681/ASN.2012030240.

[21] A. Babler, C. Schmitz, A. Buescher, M. Herrmann, F. Gremse, T. Gorgels, J. Floege, W. Jahnen-Dechent, Microvasculopathy and soft tissue calcification in mice are governed by fetuin-A, magnesium and pyrophosphate, PLoS ONE. 15 (2020). https://doi.org/10.1371/journal.pone.0228938.

[22] L.W. Zeper, J.H.F. de Baaij, Magnesium and calciprotein particles in vascular calcification: the good cop and the bad cop, Curr. Opin. Nephrol. Hypertens. 28 (2019) 368–374. https://doi.org/10.1097/MNH.0000000000000509.

[23] I. Bressendorff, D. Hansen, M. Schou, B. Silver, A. Pasch, P. Bouchelouche, L. Pedersen, L.M. Rasmussen, L. Brandi, Oral Magnesium Supplementation in Chronic Kidney Disease Stages 3 and 4: Efficacy, Safety, and Effect on Serum Calcification Propensity—A Prospective Randomized Double-Blinded Placebo-Controlled Clinical Trial, Kidney Int. Rep. 2 (2017) 380–389. https://doi.org/10.1016/j.ekir.2016.12.008.

[24] H. Quiñones, T. Hamdi, K. Sakhaee, A. Pasch, O.W. Moe, C.Y.C. Pak, Control of metabolic predisposition to cardiovascular complications of chronic kidney disease by effervescent calcium magnesium citrate: a feasibility study, J. Nephrol. 32 (2019) 93–100. https://doi.org/10.1007/s40620-018-0559-2.

[25] J.M. Diaz-Tocados, A. Peralta-Ramirez, M.E. Rodríguez-Ortiz, A.I. Raya, I. Lopez, C. Pineda, C. Herencia, A. Montes de Oca, N. Vergara, S. Steppan, M.V. Pendon-Ruiz de Mier, P. Buendía, A. Carmona, J. Carracedo, J.F. Alcalá-Díaz, J. Frazao, J.M. Martínez-Moreno, A. Canalejo, A. Felsenfeld, M. Rodriguez, E. Aguilera-Tejero, Y. Almadén, J.R. Muñoz-Castañeda, Dietary magnesium supplementation prevents and reverses vascular and soft tissue calcifications in uremic rats, Kidney Int. 92 (2017) 1084–1099. https://doi.org/10.1016/j.kint.2017.04.011.

[26] I. Bressendorff, D. Hansen, M. Schou, A. Pasch, L. Brandi, The Effect of Increasing Dialysate Magnesium on Serum Calcification Propensity in Subjects with End Stage Kidney Disease, Clin. J. Am. Soc. Nephrol. CJASN. 13 (2018) 1373–1380. https://doi.org/10.2215/CJN.13921217.

[27] I. Bressendorff, D. Hansen, A. Pasch, S.G. Holt, M. Schou, L. Brandi, E.R. Smith, The effect of increasing dialysate magnesium on calciprotein particles, inflammation and bone markers: post hoc analysis from a randomized controlled clinical trial, Nephrol. Dial. Transplant. Off. Publ. Eur. Dial. Transpl. Assoc. - Eur. Ren. Assoc. (2019). https://doi.org/10.1093/ndt/gfz234.

[28] A.D. ter Braake, C. Eelderink, L.W. Zeper, A. Pasch, S.J.L. Bakker, M.H. de Borst, J.G.J. Hoenderop, J.H.F. de Baaij, Calciprotein particle inhibition explains magnesium-mediated protection against vascular calcification, Nephrol. Dial. Transplant. 35 (2019) 765–773. https://doi.org/10.1093/ndt/gfz190.

[29] K.J. ter Meulen, M.J.E. Dekker, A. Pasch, N.J.H. Broers, F.M. van der Sande, J.B. van der Net, C.J.A.M. Konings, I.M. Gsponer, M.D.N. Bachtler, A. Gauly, B. Canaud, J.P. Kooman, Citric-acid dialysate improves the calcification propensity of hemodialysis patients: A multicenter prospective randomized cross-over trial, PLOS ONE. 14 (2019) e0225824. https://doi.org/10.1371/journal.pone.0225824.

[30] R. Villa-Bellosta, E. Hernández-Martínez, E. Mérida-Herrero, E. González-Parra, Impact of acetate- or citrate-acidified bicarbonate dialysate on ex vivo aorta wall calcification, Sci. Rep. 9 (2019) 11374. https://doi.org/10.1038/s41598-019-47934-7.

[31] G. Lorenz, C.C. Mayer, Q. Bachmann, S. Stryeck, M.C. Braunisch, B. Haller, J. Carbajo-Lozoya, A. Schmidt, S. Witthauer, J. Abuzahu, S. Kemmner, S. Angermann, N. Koneru, S. Wassertheurer, R. Bieber, U. Heemann, T. Madl, A. Pasch, C. Schmaderer, Acetate-free, citrate-acidified bicarbonate dialysis improves serum calcification propensity—a preliminary study, Nephrol. Dial. Transplant. 33 (2018) 2043–2051. https://doi.org/10.1093/ndt/gfy134.

[32] R. Villa-Bellosta, Vascular Calcification: Key Roles of Phosphate and Pyrophosphate, Int. J. Mol. Sci. 22 (2021) 13536. https://doi.org/10.3390/ijms222413536.

[33] R. Villa-Bellosta, J. Rivera-Torres, F.G. Osorio, R. Acín-Pérez, J.A. Enriquez, C. López-Otín, V. Andrés, Defective Extracellular Pyrophosphate Metabolism Promotes Vascular Calcification in a Mouse Model of Hutchinson-Gilford Progeria Syndrome That Is Ameliorated on Pyrophosphate Treatment, Circulation. 127 (2013) 2442–2451. https://doi.org/10.1161/CIRCULATIONAHA.112.000571.

[34] R. Villa-Bellosta, J. Egido, Phosphate, pyrophosphate, and vascular calcification: a question of balance, Eur. Heart J. 38 (2017) 1801–1804. https://doi.org/10.1093/eurheartj/ehv605.

[35] A.L. Boskey, A.S. Posner, Magnesium stabilization of amorphous calcium phosphate: A kinetic study, Mater. Res. Bull. 9 (1974) 907–916. https://doi.org/10.1016/0025-5408(74)90169-X.

[36] F. Abbona, A. Baronnet, A XRD and TEM study on the transformation of amorphous calcium phosphate in the presence of magnesium, J. Cryst. Growth. 165 (1996) 98–105. https://doi.org/10.1016/0022-0248(96)00156-X.

[37] N.C. Blumenthal, F. Betts, A.S. Posner, Stabilization of amorphous calcium phosphate by Mg and ATP, Calcif. Tissue Res. 23 (1977) 245–250. https://doi.org/10.1007/BF02012793.

[38] Y. Chen, W. Gu, H. Pan, S. Jiang, R. Tang, Stabilizing amorphous calcium phosphate phase by citrate adsorption, CrystEngComm. 16 (2014) 1864–1867. https://doi.org/10.1039/C3CE42274G.

[39] K. Chatzipanagis, M. Iafisco, T. Roncal-Herrero, M. Bilton, A. Tampieri, R. Kröger, J.M. Delgado-López, Crystallization of citrate-stabilized amorphous calcium phosphate to nanocrystalline apatite: a surface-mediated transformation, CrystEngComm. 18 (2016) 3170–3173. https://doi.org/10.1039/C6CE00521G.

[40] H. Fleisch, R.G.G. Russell, S. Bisaz, J.D. Termine, A.S. Posner, Influence of pyrophosphate on the transformation of amorphous to crystalline calcium phosphate, Calcif. Tissue Res. 2 (1968) 49–59. https://doi.org/10.1007/BF02279193.

[41] D.E. Koppel, Analysis of Macromolecular Polydispersity in Intensity Correlation Spectroscopy: The Method of Cumulants, J. Chem. Phys. 57 (1972) 4814–4820. https://doi.org/10.1063/1.1678153.

[42] C.F. Holder, R.E. Schaak, Tutorial on Powder X-ray Diffraction for Characterizing Nanoscale Materials, ACS Nano. 13 (2019) 7359–7365. https://doi.org/10.1021/acsnano.9b05157.

[43] M. Herrmann, A. Babler, I. Moshkova, F. Gremse, F. Kiessling, U. Kusebauch, V. Nelea, R. Kramann, R.L. Moritz, M.D. McKee, W. Jahnen-Dechent, Lumenal calcification and microvasculopathy in fetuin-A-deficient mice lead to multiple organ morbidity, PLOS ONE. 15 (2020) e0228503. https://doi.org/10.1371/journal.pone.0228503.

[44] C. Schäfer, A. Heiss, A. Schwarz, R. Westenfeld, M. Ketteler, J. Floege, W. Müller-Esterl, T. Schinke, W. Jahnen-Dechent, The serum protein α2–Heremans-Schmid glycoprotein/fetuin-A is a systemically acting inhibitor of ectopic calcification, J. Clin. Invest. 112 (2003) 357–366. https://doi.org/10.1172/JCI200317202.

[45] A. Chianese, M. Parisi, E. Fazio, Turbidimetry for the Estimation of Crystal Average Size, in: Ind. Cryst. Process Monit. Control, John Wiley & Sons, Ltd, 2012: pp. 29–34. https://doi.org/10.1002/9783527645206.ch4.

[46] C. Combes, C. Rey, Amorphous calcium phosphates: Synthesis, properties and uses in biomaterials, Acta Biomater. 6 (2010) 3362–3378. https://doi.org/10.1016/j.actbio.2010.02.017.

[47] C. Drouet, Apatite Formation: Why It May Not Work as Planned, and How to Conclusively Identify Apatite Compounds, BioMed Res. Int. 2013 (2013) 490946. https://doi.org/10.1155/2013/490946.

[48] I.R. Gibson, I. Rehman, S.M. Best, W. Bonfield, Characterization of the transformation from calcium-deficient apatite to beta-tricalcium phosphate, J. Mater. Sci. Mater. Med. 11 (2000) 799–804. https://doi.org/10.1023/a:1008905613182.

[49] M.A.M. Castro, T.O. Portela, G.S. Correa, M.M. Oliveira, J.H.G. Rangel, S.F. Rodrigues, J.M.R. Mercury, Synthesis of hydroxyapatite by hydrothermal and microwave irradiation methods from biogenic calcium source varying pH and synthesis time, Bol. Soc. Esp. Cerámica Vidr. 61 (2022) 35–41. https://doi.org/10.1016/j.bsecv.2020.06.003.

[50] S.V. Dorozhkin, Calcium orthophosphates (CaPO4): occurrence and properties, Prog. Biomater. 5 (2016) 9–70. https://doi.org/10.1007/s40204-015-0045-z.

[51] R. Gelli, M. Scudero, L. Gigli, M. Severi, M. Bonini, F. Ridi, P. Baglioni, Effect of pH and Mg2+ on Amorphous Magnesium-Calcium Phosphate (AMCP) stability, J. Colloid Interface Sci. 531 (2018) 681–692. https://doi.org/10.1016/j.jcis.2018.07.102.

[52] C. Holt, M. Van Kemenade, J.E. Harries, L.S. Nelson, R.T. Bailey, D.W.L. Hukins, S.S. Hasnain, P.L. De Bruyn, Preparation of amorphous calcium-magnesium phosphates at pH 7 and characterization by x-ray absorption and fourier transform infrared spectroscopy, J. Cryst. Growth. 92 (1988) 239–252. https://doi.org/10.1016/0022-0248(88)90455-1.

[53] J.D. Rimer, K. Sakhaee, N.M. Maalouf, Citrate therapy for calcium phosphate stones, Curr. Opin. Nephrol. Hypertens. 28 (2019) 130–139. https://doi.org/10.1097/MNH.0000000000000474.

[54] P. Gras, C. Rey, O. Marsan, S. Sarda, C. Combes, Synthesis and Characterisation of Hydrated Calcium Pyrophosphate Phases of Biological Interest, Eur J Inorg Chem. (2013) 10.

[55] Halite R070534 - RRUFF Database: Raman, X-ray, Infrared, and Chemistry, (n.d.). https://rruff.info/Halite/R070534.

[56] R. Gelli, L. Briccolani-Bandini, M. Pagliai, G. Cardini, F. Ridi, P. Baglioni, Exploring the effect of Mg2+ substitution on amorphous calcium phosphate nanoparticles, J. Colloid Interface Sci. 606 (2022) 444–453. https://doi.org/10.1016/j.jcis.2021.08.033.